Freeze-casting of highly porous cellulose-nanofiber-reinforced $\gamma-Al_2O_3$ monoliths

H. Hudelja [a,b,*], T. Konegger [c], B. Wicklein [d], J. Čretnik [e], F. Akhtar [f], A. Kocjan [a,b,*]

[a] Department for Nanostructured Materials, Jožef Stefan Institute, Jamova 39, 1000, Ljubljana, Slovenia
[b] Jožef Stefan International Postgraduate School, Jamova 39, 1000, Ljubljana, Slovenia
[c] Institute of Chemical Technologies and Analytics, TU Wien, Getreidemarkt 9/164-CT, A-1060, Vienna, Austria
[d] Instituto de Ciencia de Materiales de Madrid (ICMM), Consejo Superior de Investigaciones Científicas (CSIC), Calle Sor Juana Inés de la Cruz, 3, Madrid, 28049, Spain
[e] Slovenian National Building and Civil Engineering Institute, Dimičeva ulica 12, 1000, Ljubljana, Slovenia
[f] Division of Material Science, Luleå University of Technology, SE-97187, Luleå, Sweden

A B S T R A C T

Freeze-casting is a powerful consolidation technique for the fabrication of highly porous and layered-hybrid materials, including ceramic-metal composites, and porous scaffolds for catalysis, bone substitutes and high-performance membranes. The aqueous suspensions to be freeze-casted usually contain dense particles facilitating macroporous, layered ceramics with dense (nonporous) struts. In the present study, hierarchical macro-mesoporous alumina (HMMA) monoliths were successfully prepared by freeze-casting of aqueous suspensions containing hierarchically-assembled, mesoporous $\gamma-Al_2O_3$ (MA) powder and cellulose nanofibers (CNF). As-prepared monoliths were ultra-porous (93.1–99.2%), had low densities (0.01–0.25 g/cm³), and displayed relatively high surface areas (91–134 m²/g), but were still remarkably rigid with high compressive strengths (up to 52 kPa). Owing to the columnar porosity and mesoporous nature of the struts the freeze-casted HMMA monoliths exhibited high permeability and high thermal insulation, the latter ranging from 0.039 W/m·K to 0.071 W/m·K, depending on pore orientation.

1. Introduction

Traditional macroporous ceramics are a class of materials important in many technological solutions when it comes to applications related to catalysis, filtration, high-temperature thermal insulators, light-weight structural components and biomedicine [1,2]. Moreover, the benefits of introducing hierarchical porosity have recently been recognized. The presence of macropores considerably improves mass transport capacity and the material's diffusion properties [3–5]. On the other hand, introduction of mesoporosity considerably increases the available specific surface area of the monolith, thus enhancing the number of active sites [4,6].

Alumina is one of the most widely used porous ceramics [7]. Especially in its gamma crystallographic form ($\gamma-Al_2O_3$), the resultant mesoporous alumina (MA) has many unique properties such as nanocrystallite size, high mesoporosity, large surface area, high surface density of the hydroxyl groups, and low thermal conductivity [8]. $\gamma-Al_2O_3$ is regarded as an ideal candidate for the preparation of

hierarchically macro-mesoporous alumina (HMMAs) materials [9–11]. There are two commonly used procedures for the fabrication of HMMA monoliths. The first one is a combination of sol-gel synthesis of MA [12,13] and phase separation, i.e. macropores are generated when a phase separating agent, i.e., porogen, is added to the aluminum sol-gel precursor [6,14]. In the second procedure, a macroporous polymer template is impregnated with alumina hydrosol [15,16]. The first route, however, may suffer from cracking of the monoliths during drying [17], while in the second route, control over the macropore insertion is difficult and requires calcination procedures for removal of the sacrificial template that can negatively affect the surface features.

On the verge of the 21st century, freeze-casting (FC), also known as ice templating, was established as a powerful consolidation technique for the fabrication of sophisticated (macro)porous and layered-hybrid materials [18–20] and would as such be potentially suitable for the preparation of HMMA. Such layered-porous materials show potential as catalyst support adsorption and chromatography [27]. The layered nature of the FC porous monoliths, not being as tortuous as those prepared

---

by porogens, is beneficial when high flow/pressure of gas is applied thus reducing the pressure drop. Several studies can be found on FC of aqueous suspensions containing non-(meso)porous alpha-alumina (α–Al_2O_3) particles [21–26]. After FC consolidation and sintering, the obtained monoliths are always macroporous (40–95%), exhibiting ordered, lamellar or columnar pore structure and more or less dense struts.

A recent study of Dhainaut et al. showed possibility to fabricate HMMA by the careful control and consecutive execution of sol-gel chemistry, surfactant self-assembly, and ice-templating, where the final properties of ice-templated monoliths are influenced by 13 interdependent parameters [5]. The influence of final calcinating step, where boehmite is transformed to gamma alumina, on the mechanical properties (degradation) of monoliths was not discussed. While this study importantly implements the structuring of HMMA from boehmite sols excluding the need of using porogens, the strategy employed cannot be used for structuring commercially-available MA powders, or those synthesized by other means, for example, by exploiting the AlN powder hydrolysis [27,28], and other difficult-to-consolidate porous materials without calcinating/sintering steps, such as zeolites. Ojuva et al. successfully structured zeolite 13X monoliths with a laminated structure and hierarchical macro/microporosity by FC colloidally stable aqueous suspensions of zeolite powder, bentonite, and polyethylene glycol. For achieving mechanically stable zeolite 13X monoliths thermal treatment at 1053 K was required were 9 and 17 wt % bentonite acted as inorganic binder [29].

Indeed, in FC process it is imperative that the aqueous suspensions to be freeze-casted are colloidally stable and are not prone to agglomeration, segregation, or sedimentation. In a recent study we have shown how it is possible to prepare stable, highly loaded aqueous suspensions containing AlN-hydrolysed, hierarchically assembled MA powder with high surface area [30]. With the addition of sufficient amounts (>1 wt%) of cellulose nanofibers (CNF), interparticle association (networks) between sodium polyacrylate (NaPAA) stabilized MA particles and CNF was triggered. As a result, stable suspensions neither prone to sedimentation nor particle segregation over longer time periods (more than 12 weeks) were prepared.

The present follow up study was designed to employ, for the first time, the above mentioned aqueous interparticle associations of hierarchically-assembled MA particles and CNF in the FC process in order to prepare mechanically stable, highly-porous HMMA ceramic monoliths not requiring calcination nor sintering step. The goal was to freeze cast a hierarchically porous material exhibiting reasonable mechanical properties, low thermal conductivity and high permeability, suitable for high flow applications. The influence of individual processing parameters such as MA powder volume fraction, CNF content and freezing rate, on porosity, permeability, insulative and mechanical properties of fabricated HMMA monoliths was studied in detail.

2. Materials and methods

2.1. Preparation of starting materials

2.1.1. Synthesis of MA powder

Hydrolysis of AlN (Grade C, H.C. Starck, Germany) was used to prepare the MA powder. Distilled water was heated to the boiling point in a glass beaker, then AlN powder (10 wt%) was added during constant mixing. The beaker was covered, placed in an oven and left to boil for 7 h. After 7 h, the suspension was filtered (filter paper Grade 393, Sartorius AG, Germany), washed with isopropanol, and dried at 120 °C for 24 h. The dried powder was sieved (mesh 230) and treated in air at 500 °C for 1 h (heating rate 10 °C/min). The as-prepared MA powder consisted of hierarchically assembled, globular micron-sized aggregates with a mean particle size of 8.9 μm. MA powder also displayed high mesoporosity (0.47 mL/g) and a relatively high surface area of 180 m^2/g. A detailed description of the synthesis path and characterization of as-synthesized MA powder can be found elsewhere [30].

Table 1

Overview of suspension parameters and consolidation conditions used in freeze-casting.

Sample	MA volume fraction (ϕ_A)[a]	γ_{MA} (g/mL)[b]	w_{CNF} (wt%)[c]	γ_{CNF} (mg/mL)[b]	Freezing rate (°C/min)
FZC–2	0.013	0.046	10.0	4.6	1
FZC–3	0.013	0.046	10.0	4.6	6
FZC–4	0.027	0.092	5.0	4.6	1
FZC–5	0.027	0.092	7.0	6.6	1
FZC–6	0.027	0.092	7.0	6.6	6
FZC–7	0.054	0.190	2.0	4.0	1
FZC–8	0.054	0.190	2.0	4.0	6
FZC–9	0.082	0.289	1.0	3.0	1

[a] Volume of MA powder was calculated using apparent density (ρ_A) of 3.35 g/mL [30].

[b] γ_{MA} and γ_{CNF} are mass concentrations of MA powder and CNF, respectively (mass per 1 mL of suspension).

[c] Mass fraction of CNF was determined according to equation: $w_{CNF} = m_{CNF}/(m_{CNF} + m_{MA}) \cdot 100$.

2.1.2. Cellulose nanofiber gel preparation

Cellulose nanofibers (CNF) were extracted from bleached *Eucalyptus globulus* kraft pulp. An aqueous wood pulp suspension was chemo-mechanically nanofibrillated by TEMPO-mediated oxidation in combination with defibrillation in a high-pressure microfluidizer (Microfluidics Corp., USA). As a result a 1.55 wt% CNF gel with carboxylated nanofibers (900 μmol/g charge) and approximate fiber thickness of $\approx$ 2 nm was obtained [31].

2.2. Freeze-casting process

2.2.1. Preparation of MA-CNF aqueous suspensions

Suspensions were prepared as follows: 1.4 wt% of sodium polyacrylate (MW 225 000, 20 wt% aqueous solution), obtained from Polysciences Europe GmbH, Germany, and a predetermined quantity of distilled water were added to a plastic bottle and mixed with a magnetic stirrer. In the second step the CNF in mass fraction (w_{CNF}) between 1 and 10% was added into the water solution of sodium polyacrylate (NaPAA) and thoroughly mixed again. Subsequently, the MA powder in volume fractions (φ_A) between 0.013 and 0.082 was slowly added during mixing. For calculation of φ_A apparent density (ρ_A) was used (3.35 g/mL) [30]. The suspensions were homogenized in a slow 24 h ball milling. Zirconia balls of 10 mm diameter were used (approximately 2 balls per 10 mL of suspension). In the last step, where needed, NaOH (Neolab Migge GmbH, Germany) was added to set the pH value to 9 (SevenMulti pH meter equipped with an InLab expert pro electrode, Mettler Toledo, International Inc., USA).

For all suspensions, except FZC–1, amounts of NaPAA and CNF were calculated based on the mass of dry MA powder. Components amounts, i.e., mass fractions of NaPAA and CNF, for preparation of FZC–1 (prepared without MA powder), were calculated based on mass of water instead of dry MA powder. The suspension FZC–1 was prepared with the following ratio: per 10 mL of water 0.013 g of NaPAA and 0.066 g of CNF were added (masses of CNF and NaPAA per 10 mL of suspension were the same as in the case of monolith FZC-5). Monoliths FZC–1 were frozen at the rate of 1 °C/min.

2.2.2. Freeze-casting process

In Table 1 an overview of suspensions parameters used for the freeze-casting process is given. Since the monoliths FZC–1 were prepared without MA powder, their preparation parameters were not included in Table 1.

For freeze-casting, suspensions were poured in either a cylindrical PTFE mold with inner diameters of 25 mm ($V_{susp} \approx$ 16 mL) or 10 mm ($V_{susp} \approx$ 1.5 mL) or in a square shaped PTFE mold with a side length of 20 mm ($V_{susp} \approx$ 10 mL). The mold was placed on top of a copper rod
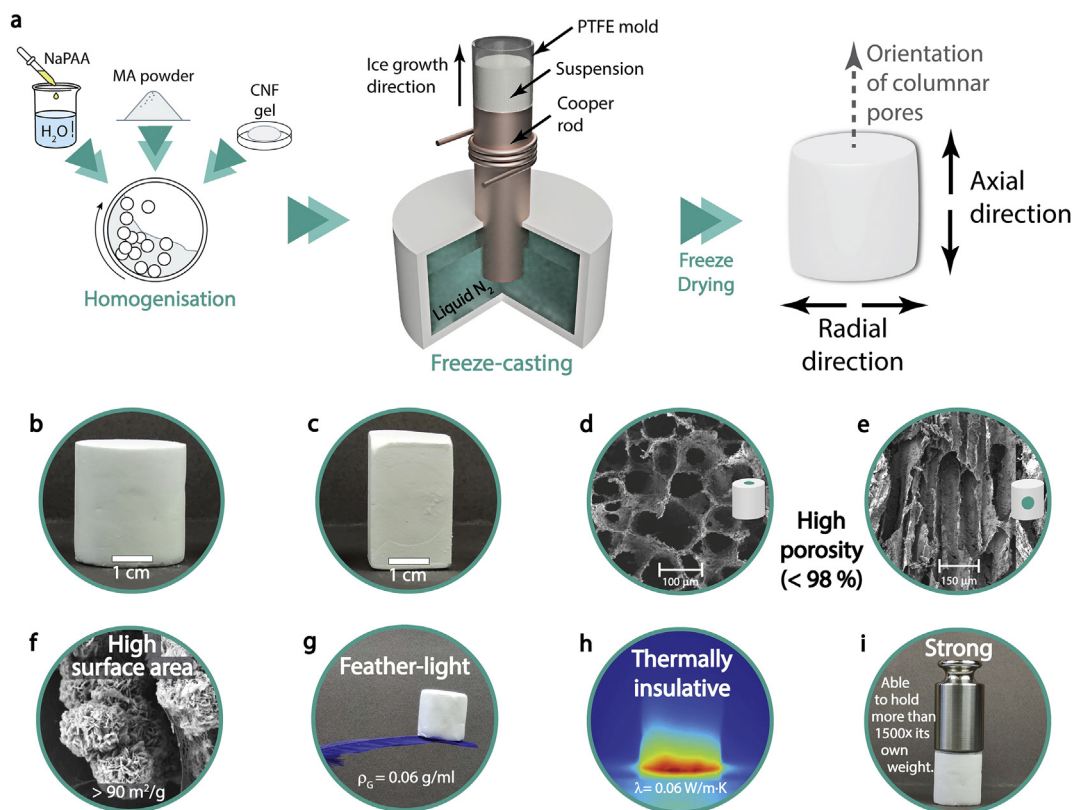
Fig. 1. Illustration of consolidation process with emphasis on key-properties of as-prepared monoliths. **a,** Illustration of freeze-casting process. **b,** Cylindrical-like monolith after freeze drying. **c,** Cuboid-like monolith after freeze drying. **d,** SEM of monolith FZC–5, which contained $\phi_A = 0.027$ of MA powder and 7 wt% CNF (Table 1) viewed in axial direction (top view). **e,** SEM of monolith FZC–5 viewed in radial direction (side view). **f,** SEM of monolith showing high surface area, originating from hierarchical assembly of 2D-nanosheets during AlN-hydrolysis. **g,** Freeze-casted monolith can be placed on a tip of a feather. **h,** Monolith FZC–5, showed excellent thermal insulation. **i,** Monolith FZC–5, with $\rho_G = 0.11$ g/cm^3 can sustain more than 1500 times its own weight.

immersed in liquid nitrogen (Fig. 1a). The temperature at the top of the rod was controlled with the help of a thermometer and a heating ring. Suspensions were freeze-casted at two different (linear) freezing regimes (1 K/min or 6 K/min). The starting temperature of the copper rod was 5 °C, while the end temperature was −50 °C. Freeze-casted samples were taken from the mold and placed in a freeze dryer (2–4 LSCbasic, Martin Christ Gefriertrocknungsanlagen GmbH, Germany) set to T = −80 °C and p = 0.001 mbar for the ice to sublimate.

For comparison, dry-pressed disk-shaped specimens were prepared. For this purpose, synthesized MA powder was dried at 200 °C and then firstly uniaxially dry-pressed in a steel die of 25 mm diameter at 100 MPa, followed by a subsequent cold isostatic pressing (CIP) step using a final pressure of 200 MPa (MA–CIP200). Preparation and characterization of monoliths via CIP of hydrolysis-derived-MA powder was already reported elsewhere [32].

2.3. Characterization of freeze-casted monoliths

All samples were conditioned in a vacuum dryer at 40 °C for at least 24 h prior to all the measurements. Also if not otherwise stated aside from drying, no sample treatment was carried out prior to analyses.

Scanning electron microscopy (SEM; ULTRA plus, Carl Zeiss SMT, Germany) was used to characterize the shape of the pores in freeze-casted samples. Due to low conductivity, samples were coated with gold prior to analysis. The SEM analysis was performed at an accelerating voltage of 5 kV. For the SEM analysis, sections of monoliths were cut with a sharp scalpel perpendicular and parallel to the ice growth direction. Therefore, axial direction is parallel to the orientation of columnar pores, while the radial direction is perpendicular to it (Fig. 1a).

Nitrogen adsorption/desorption isotherms were obtained using a

nitrogen-sorption analyzer (Nova 2000e, Quantachrome GmbH & Co. KG, USA). The Brunauer–Emmett–Teller (BET) equation with the data in the P/P_0 range of 0.01–0.3 was used for calculations of the specific surface areas. For analyses cylindrical monoliths with a diameter of 10 mm and height of 20 mm were used. To accommodate the dimensions of measuring cell, the monoliths were first cut in half in radial direction and then each half was additionally cut into four pieces in axial direction. All pieces were placed into a measuring cell and degassed at 150 °C for 24 h prior to the measurement. One measurement per batch was carried out.

Mercury-intrusion porosimetry (Pascal 140 and Pascal 440, Thermo Fisher Scientific, USA), with pressures from 10 kPa up to 400 MPa (corresponding to a pore diameter interval from 115 μm to 3.2 nm) was used to determine the porosities and pore size distribution of green bodies and pure MA powder. The surface tension and the contact angle of the mercury were set to standard values of 0.485 mN/m and 130°, respectively. Two measurements were carried out for each of the samples and the results are given as an average value. Dimensions of monoliths were adjusted so that the volume of pores was between approximately 250 and 350 mm^3. Cylinders with a diameter of 10 mm were used. Their height was first adjusted to 14 mm (by cutting of equal parts from the upper and bottom side). Then individual pieces were also cut in axial direction into three approximately equal parts. For analysis of FZC–1, FZC–2 and FZC–3 all three parts had to be used to achieve adequate volume of pores, while for other monolith only one third was enough.

Geometric densities (ρ_G) were calculated by weighing the monoliths (with a precision of ±0.001 g) and measuring their volume. Volume was estimated by measuring the height and the diameter of one cylindrical monolith (diameter of 25 mm) and one cubic monolith (side of 20 mm) with a digital caliper (with a precision of ±0.01 mm). Where needed, the upper surface of monolith was gently polished using silicon carbide
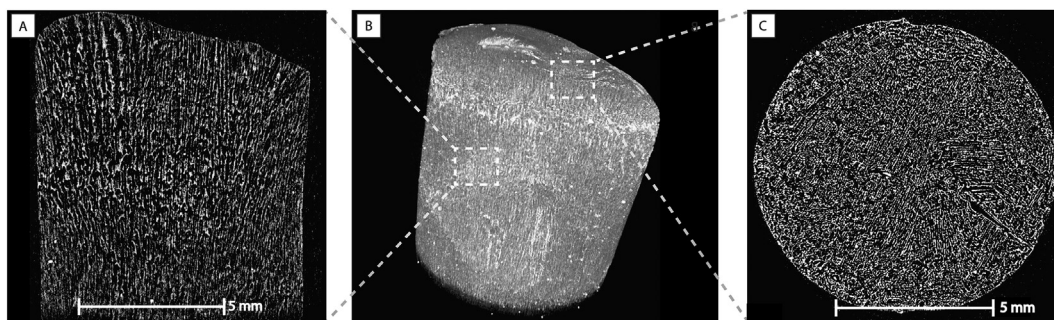
Fig. 2. A) μ–CT of monolith FZC–5 viewed in radial direction. **B)** μ–CT of monolith FZC–5 viewed in 3D. **C)** μ–CT of monolith FZC–5 viewed in axial direction.

grinding paper (2400 grit) to make it parallel to the bottom plate. The average value of ρ_G is given as a result.

Monoliths with a diameter of 10 mm and approximate height of 15 mm were used to perform X-ray micro-computed tomography (μ–CT). XRadia MicroXCT-400 tomograph (XRadia, Concord,CA, USA) was used to investigate the structural characteristics of the specimens. The beam energy and the intensity were set to 40 kV and 176 μA, respectively. No filter was used. With this method, 500 projection images at an exposure time of 5 s per projection were acquired on the charge-coupled device (CCD) camera, where the resolution of scanned samples using macro objective (0.39×) was 10.6 μm for one pixel.

The thermal conductivity (λ) and specific heat capacity (c_p) of CIP or freeze-casted monoliths were measured with a Hot Disk thermal constant analyzer TPS 2500 S (HotDisk AB, Gothenburg, Sweden). A 6.4 mm Kapton sensor, sandwiched between a pair of cylindrical/cubic samples, was used for the determination of λ. Where needed, the upper surface of monolith was gently polished using silicon carbide grinding paper (2400 grit) to make it parallel to the bottom plate. The measurements were performed in the anisotropic module. The specific heat capacity of the monoliths was determined using a special sensor-cell, consisting of an insulated hollow gold cylinder. The average values were calculated from five measurements per sample with a 1-h conditioning time between individual measurements for thermal conductivity and 2-h conditioning time for heat capacity measurements. A detailed description of the experimental process can be found in the Supplementary Material.

Thermographic images were captured with an infrared thermal camera (Fluke Ti55FT IR FlexCam) with a thermal sensitivity of 0.05 °C. Cylindrical samples (diameter of 25 mm and approximate height of 25 mm) were placed on a stage made of mullite fiber wool. A round hole was made in the middle of the wool for the heating source (a small copper cylinder with diameter of 10 mm). The temperature at the top of copper cylinder was approximately 180 °C.

Permeability testing was conducted at room temperature using cylindrical samples with a diameter of 10 mm and a height of 25–30 mm, with filtered compressed air as fluid. The specimens were radially sealed

using heat shrink tubing. The stationary permeating gas flow Q was recorded as a function of differential pressure Δp between upstream and downstream side of the specimen. A minimum of 12 sets of pressure drop and Q values were recorded per sample in the Δp range between 0.6 and up to 2.4 bar, the maximum pressure depending on sample integrity during testing. Three samples were tested per batch. Darcian (k_1) and non-Darcian permeability (k_2) were determined based on Forchheimer's equation for compressible fluids [33], shown in Eq. 1 (Supplementary Material).

The compressive strength measurements were performed using Quasar 100 (Galdabini, Cardano al Campo, Italy) with a 100 N load cell. Cylinders with a diameter of 25 mm and an approximate height of 25 mm or cubic monoliths with a side length of 20 mm were used to determine compressive behaviour in axial and radial direction in regard to the ice-growth direction, respectively. The monoliths were compressed at a constant speed of 0.5 mm/min. Two samples were tested for each batch and the results were averaged. Results where only one sample per batch was compressed are clearly marked (Table S3, Supplementary Material). Since maximum two samples per batch were tested, the obtained results should be regarded as an estimation, but are still sufficient for establishing the influence of individual processing parameters on compressive properties.

3. Results and discussion

The freeze-casting process (Fig. 1a) enabled the formation of cylindrical- or cuboid-like hierarchically macro-mesoporous γ–Al$_2$O$_3$ monoliths (HMMAs) (Fig. 1b and c, respectively). As-prepared HMMA monoliths exhibited columnar/channel-like porosity running parallel to the freezing direction (Fig. 1d and e), where the mesoporous struts were composed of hierarchically-assembled MA consolidated particles entangled in a CNF percolating network contributing to overall high surface area (Fig. 1f). The monoliths were highly porous i.e., up to 98.5%, and thus could be placed on a tip of a feather without bending it (Fig. 1g). Monoliths The resultant microstructural features of the as-prepared

Table 2
Summary of specific surface areas and porosities of freeze-casted monoliths.

Sample	Specific surface area (m^2/g)	Geometric density (g/cm^3)	Geometric porosity[a] (%)	Hg intrusion porosity (%)
FZC–1	45	0.011 ± 0.001	99.2 ± 0.1	96.6 ± 0.3
FZC–2	91	0.056 ± 0.002	98.5 ± 0.1	96.5 ± 0.3
FZC–3	/	0.056 ± 0.001	98.5 ± 0.0	96.1 ± 0.1
FZC–4	105	0.097 ± 0.002	97.5 ± 0.1	96.2 ± 0.6
FZC–5	100	0.108 ± 0.007	97.1 ± 0.2	96.8 ± 0.2
FZC–6	117	0.109 ± 0.010	97.1 ± 0.3	96.2 ± 0.4
FZC–7	128	0.172 ± 0.006	95.6 ± 0.2	94.4 ± 0.5
FZC–8	138	0.177 ± 0.003	95.4 ± 0.1	94.3 ± 0.1
FZC–9	134	0.272 ± 0.002	93.1 ± 0.1	90.8 ± 0.9[b]
MA–CIP200	138	1.158 ± 0.003	70.7 ± 0.1	71.0 ± 0.1

[a] Calculated as $(1-\rho_{rel}) \cdot 100\%$; ρ_{rel} is the relative density and is calculated as ρ_{geom}/ρ_{theor}; theoretical density was estimated from mass fractions and densities of the components; values $\rho_{CNF} = 1.46$ g/cm^3, $\rho_{MA} = 3.95$ g/cm^3 were used.

[b] Sample was partly crushed during measurement. Results should be interpreted carefully.
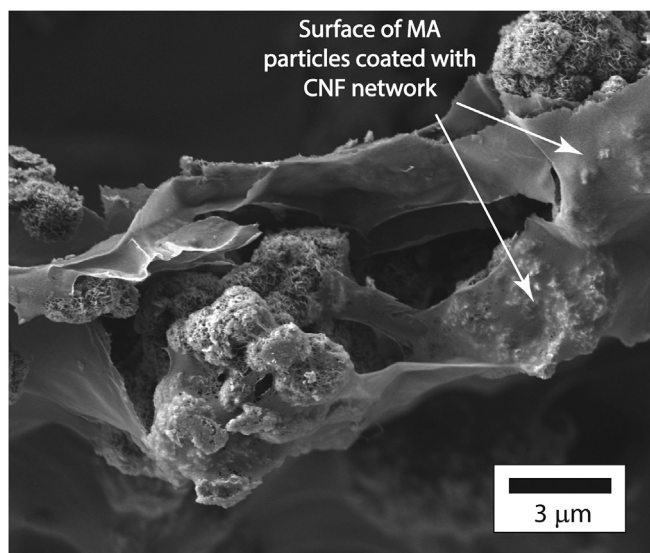
Fig. 3. SEM image showing MA particle entrapped in CNF network.

ceramic "foams" contributed to the excellent insulative properties with average thermal conductivity value as low as 0.06 ± 0.003 W/m·K (Fig. 1h) and to a high stiffness, since they were able to hold up to 1500 times their own weight (Fig. 1i).

3.1. Structural characterization

Porous materials, prepared by unidirectional freezing of aqueous suspensions, are distinguished by an evolution of pore channels, which are a replica of the ice crystals formed during freezing [18,34].

When a unidirectional freezing temperature gradient is applied to the suspension, the growth of ice crystals is not random, but rather directional, i.e. they are forced to grow along the temperature gradient [18]. As a consequence, pore channels with long-range order run continuously along one axis of the monolith, that is from the bottom to the top [35]. Evolution of such ordered pore channels, i.e. columnar porosity in HMMAs running parallel to the ice growth direction was confirmed by μ–CT analysis (Fig. 2A and B). A more detailed investigation of μ–CT images taken perpendicular to ice-growth (Fig. 2C) showed that the structure was not completely random, but exhibited some short-range order. Smaller sections in which pore walls were locally aligned could be observed, but no long-range order was present. Such randomly
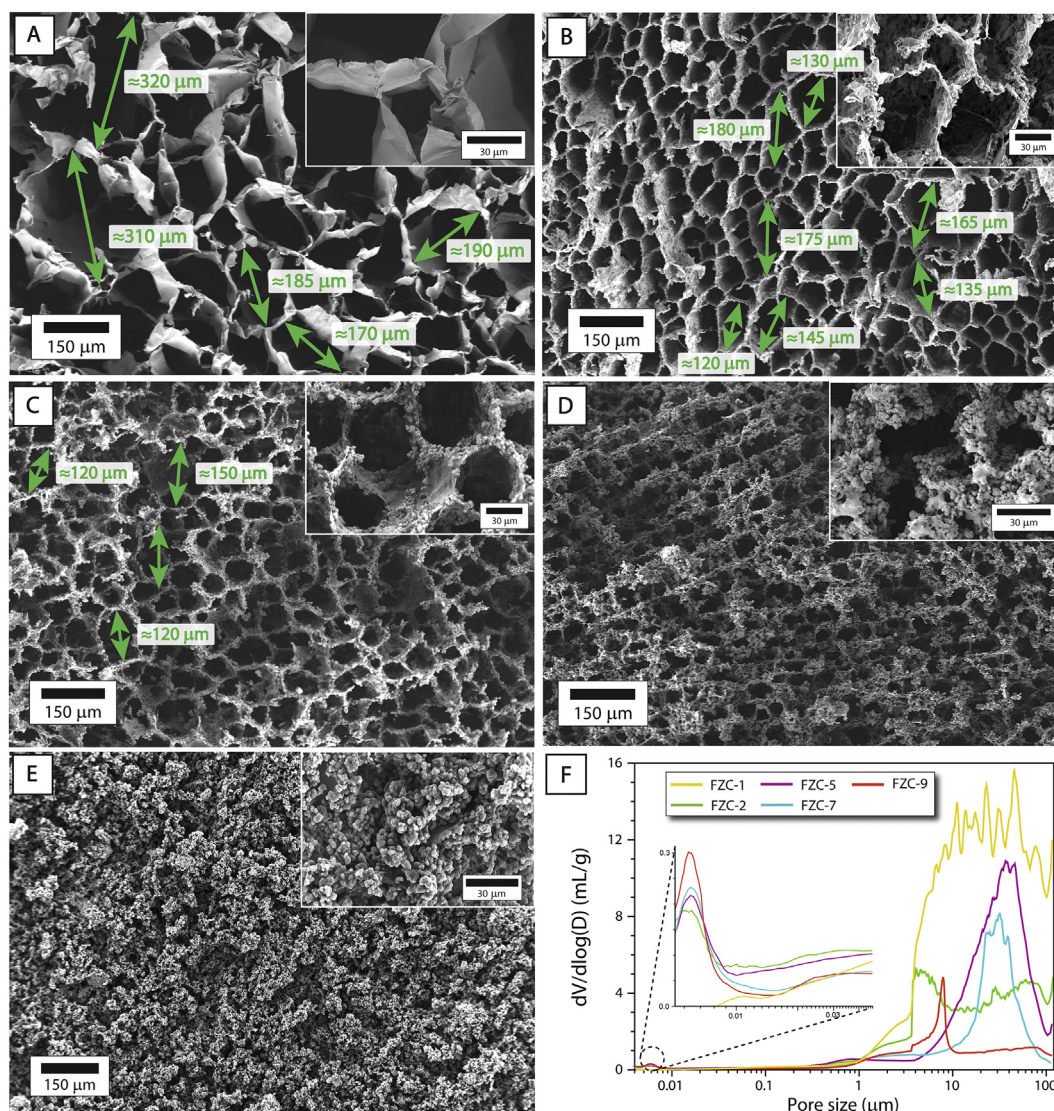
Fig. 4. SEM images of A) monolith FZC–1, B) monolith FZC–2, C) monolith FZC–5, D) monolith FZC–7, E) monolith FZC–9, all viewed in axial direction. F) Influence of MA powder volume fraction on pore size distribution in samples frozen at 1 °C/min. Arrows indicate pores bigger than 115 μm.

orientated domains, containing organized lamellae, are characteristic for monoliths frozen on a cold finger with a smooth surface [18,36].

Geometric densities were between 0.056 and 0.272 g/cm^3 for freeze-casted monoliths containing MA powder. This corresponded to porosities as high as 98.5% (Table 2). Additionally, an increase in MA volume fraction caused the expected trend of increasing density (ρ_G) and decreasing porosity. The density of monolith FZC–1 (prepared without MA powder) was considerably lower (0.011 g/cm^3) and comparable to the already reported densities of CNF aerogels [37,38].

A trend of increasing specific surface area (SSA) with an increasing MA/CNF ratio can be observed (Table 2). Additionally, when comparing SSA of two monoliths with the same MA/CNF ratio, but frozen at two different rates (FZC–5/FZC–6 and FZC–7/FZC–8) a considerably higher surface area is obtained for monolith frozen at faster rate. The latter is to be expected, since faster cooling rate results in smaller pores and thus in higher (macro)pore surface area (Fig. S2, Supplementary Material). The surface areas of monoliths containing MA powder (FZC–2 to FZC–9) were in the range of 91–134 m^2/g, while for monolith containing only CNF and NaPAA (FZC–1) SSA was much lower SSA ($\approx$45 m^2/g). A portion of the surface area, possessed by the pure MA powder (180 m^2/g) [30], was likely lost due to a partial coverage of the MA surface by the CNF network (Fig. 3).

SEM imaging (Fig. 4A–E) confirmed μ–CT findings, that is, that in the majority of the monoliths columnar pores were formed. With increasing MA powder volume fraction, pore sizes started to decrease, pore walls started to thicken, and the columnar structure became less distinct. At φ_A = 0.054, columnar porosity was still present, but its shape was no longer as well defined (Fig. 4D) as in monoliths containing lower MA volume fractions (Fig. 4B and C). At φ_A = 0.082, the volume fraction was too high to enable formation of columnar porosity and walls (Fig. 4E). The gradual transition from columnar porosity to randomly shaped pores was probably related to an insufficient mobility of the dispersed particles which led to an early entrapment of the suspended particles in the advancing freezing front [35] and to a randomly shaped pores.

Due to the intrinsic mesoporosity of MA powder, monoliths FZC–2 through FZC–9 also possessed a substantial amount of mesopores (approximate value of 0.12 cm^3/g, with the average pore diameter of 6 nm) beside macropores, i.e. they were hierarchically porous (inset of Fig. 4F). Presence of CNF, which on its own possessed almost no mesoporosity ($\approx$0.03 cm^3/g for monolith FZC–1), was apparently responsible for the decreased mesoporosity of HMMAs in comparison to the pure MA powder, which possessed the mesopore volume of 0.27 cm^3/g (Fig. S1J, Supplementary Material).

The expected trend of decreasing porosity with increasing MA volume fraction can indeed be observed (Fig. 4F and Table 2). However, there were slight deviations at lower volume fractions (φ_A < 0.054). Porosities determined by Hg intrusion were lower at lower MA volume fractions, when they should have increased with decreasing solid content [22]. A closer look at intrusion curves showed that in the case of φ_A < 0.054 there was a sharp increase of the dV/dlog(D) curve at pore diameters above 100 μm (Fig. 4F). This indicates that there were pores larger than 115 μm, i.e. larger than the detection limit. The presence of the latter was additionally confirmed by SEM (Fig. 4, A–C). Consequently, porosities determined by this method were lower that the real values. Geometrically determined porosities (Table 2) were closer to the true values and followed the expected trend. The mentioned rise of the intrusion curves at pore diameters of $\approx$115 μm was however not observed for monoliths FZC–7 and FZC–9, indicating that pores exceeding 115 μm were not formed. Consequently, the match between geometrically and Hg-intrusion determined porosities was much better (almost identical) at higher MA volume fractions, while substantial differences could be observed for lower volume fractions.

Monolith FZC–1 (prepared without MA powder) had the widest pore size distribution (from 1 μm to well over 115 μm) with the biggest pores (up to 320 μm), as can be seen from Fig. 4A and F. While the pore size distribution of monolith FZC–2 was still very broad (comparable to FZC–

Table 3
Summary of air permeability characteristics of HMMA.

Monolith	No. of samples	$k_1/\times 10^{-12}$ m^2	$k_2/\times 10^{-7}$ m
FZC-5	3	2.39 ± 0.19	9.15 ± 6.51
FZC-7	3	4.31 ± 0.47	2.23 ± 0.26

1), the pores were slightly smaller, with the largest pores detected around 180 μm (Fig. 4B). On the other hand, a much narrower pore size distribution can be observed for monoliths with $\phi_A \geq$ 0.054. The modal pore diameter of monolith FZC–5 was 40.5 μm, while for FZC–7 the size distribution was even narrower, with a slightly lower modal pore diameter appearing at 29.7 μm. The narrowest pore size distribution was detected in monolith FZC–9, with the main peak at a much lower diameter (7.8 μm). Additionally, with increasing MA volume fraction the number of pores exceeding 115 μm decreased, until the volume fraction was high enough ($\varphi_A \geq$ 0.054) to entirely prevent their formation.

3.2. Permeability

Materials with high, columnar porosity are usually distinguished by improved gas permeability [39,40]. Thus Darcian (k_1) and Non-Darcian (k_2) permeability were determined for monoliths FZC–5 and FZC–7. Both the Darcian permeability (corresponding to a viscous flow regime) and the Non-Darcian permeability (corresponding to inertial effects) were determined based on Forchheimer's equation for compressible fluids (Eq. 1, Supplementary Material). The k_1 and k_2 values found for monoliths generated in this work were comparable to the ones obtained for freeze casted and sintered alumina monoliths [41] and to the typical values encountered for fibrous filters [33]. On the other hand, their permeability was considerably better than the permeability of alumina foams [42] or HMMAs prepared by cold isostatic pressing of the same MA powder as used in this study (k_1 = 0.08–22.1 × 10^{-16} m^2, k_2 = 0.03–5390 × 10^{-15} m) [32].

Variation of k_1 values between monoliths of the same batch was relatively low, indicating a good reproducibility of permeability characteristics. The k_1 of monolith FZC–7 was somewhat higher than that of monolith FZC–5 (4.31 × 10^{-12} and 2.39 × 10^{-12}, respectively, Table 3), while the Non-Darcian permeability contributions seemed to be higher for FZC–5 (9.15 × 10^{-7} in comparison to 2.23 × 10^{-7} for monoliths FZC–7). While k_1 is mostly dependent on sample porosity and pore size, k_2 is also sensitive to the changes in flow and velocity of gas molecules [41]. Since the porosities and pore size distribution of monoliths FZC–5 and FZC–7 were relatively similar (Fig. 4F and Table 2), the differences between k_1 values were also relatively small. On the other hand, there is more than 300% difference between Non-Darcian permeability. From SEM images (Fig. 4C and D), a clear transition from a columnar structure (FZC–5) to more randomly shaped pores (FZC–7) can be observed. Since the pores in the case of monolith FZC–5 exhibited a higher alignment, i.e., were less tortuous, the air flow was less obstructed and the resulting permeability was higher.

However, a rather high error in the determination of k_2 for monolith FZC–5 should not be overlooked (Table 3). The error of k_2 value for monolith FZC–5 could be related to the rather limited monolith strength observed during permeability measurement. The latter may have led to potential warping or degradation of the monoliths and consequently affected the flow and velocity of gas molecules, which in turn affected k_2.

3.3. Mechanical properties

Fig. 5A and B shows the stress-strain curves of monoliths containing different MA volume fractions and CNF contents. Due to the anisotropic structure (Fig. 4A–D), selected monoliths were compressed in axial as well as in radial direction in order to establish the influence of pore orientation (Fig. 5B). The curves had a shape typical for porous monoliths containing cellulose [43]. At low strains, a linear elastic region can be
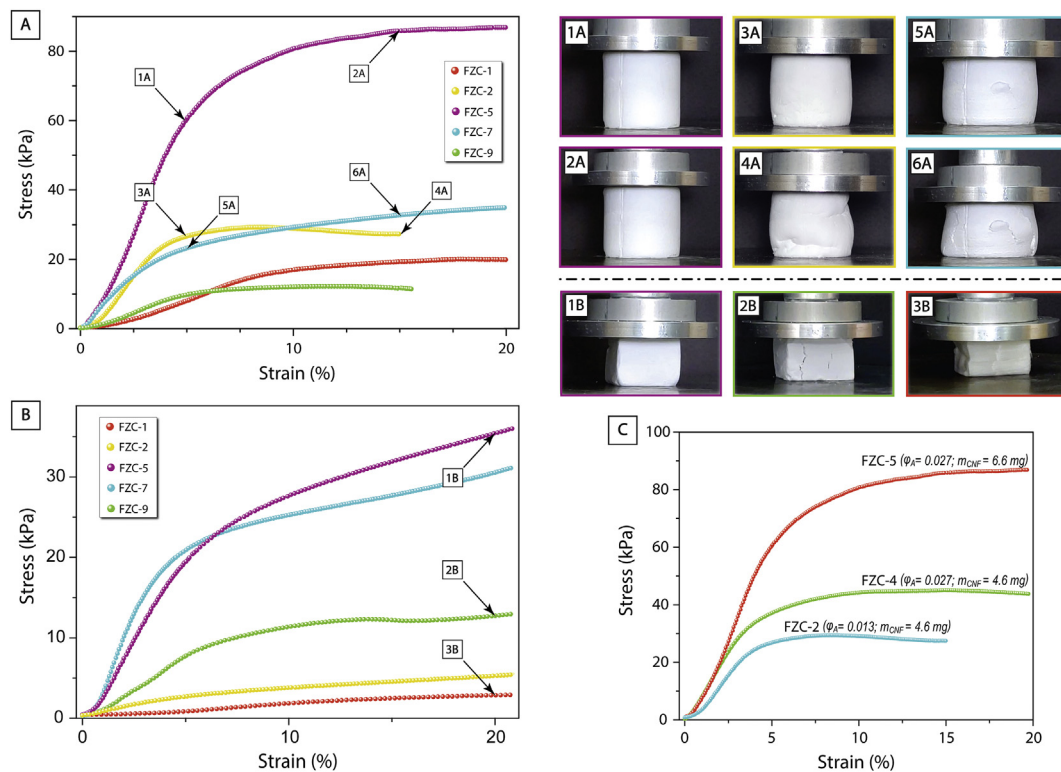
Fig. 5. A) Stress-strain curves of monoliths prepared with different contents of MA powder and CNF, measured in axial direction. B) Stress-strain curves of monoliths prepared with different contents of MA powder and CNF, measured in radial direction. Pictures 1A–6A show monoliths compressed in axial direction at 5 and 20% strain as indicated by the arrows, while pictures 1B–3B show monoliths compressed in radial direction at 20% strain. C) Influence of CNF content and MA volume fraction on compressive behavior (axial direction). Monoliths contained either the same amount of MA powder (FZC–4 and FZC–5) or the same amount of CNF (FZC–2 and FZC–4). Mass of CNF is given in mg of CNF per 1 mL of suspension.

Table 4
Summary of compressive properties of freeze-casted monoliths.

Sample	Yield point (kPa)	Young's modulus (kPa)	Yield point (kPa)	Young's modulus (kPa)
	axial direction	axial direction	radial direction	radial direction
FZC–1 [a]	4	130	1 ± 0	20 ± 10
FZC–2	20 ± 2	590 ± 20	2 ± 0	70 ± 10
FZC–3	5 ± 1	610 ± 40	/	/
FZC–4 [a]	28	930	/	/
FZC–5	52 ± 6	1080 ± 430	14 ± 0	410 ± 40
FZC–6 [a]	40	1000	/	/
FZC–7	13 ± 1	670 ± 190	12 ± 1	510 ± 110
FZC–8 [a]	14	620	/	/
FZC–9	2 ± 0	150 ± 40	2 ± 0	130 ± 60

[a] Axial compressive properties that were determined from only one monolith per batch.

observed, where deformation was mainly a consequence of pore walls elastic bending [44]. From the end of this region yield points were estimated and the compressive modulus was calculated (Table 4). The linear zone was followed by a plateau region, where the porous structure collapsed under increasing stress.

Pictures were taken during testing at different strains (10 and 15% for axial direction and 20% for radial direction), shown in Fig. 5 (pictures 1A–6A and 1B–3B, respectively). The monoliths with CNF content ≤0.4 mg/1 mL of suspension (FZC–7 and FCZ–9) cracked during compression, while the monolith containing very low MA volume fractions, i.e. $\varphi_A \leq$

0.013 (FZC–1 and FCZ–2) exhibited caving in. It thus follows that a certain ratio between MA and CNF is needed in order to achieve the best possible mechanical response in both directions. Since monolith FZC–5 showed no visible changes, i.e. cracking or caving in after compression in any of the tested directions, it follows that its mass ratio between MA and CNF was the closest to the optimal one in regards to mechanical properties (approximately 15:1). Deviations from this ratio either in the favor of CNF or MA powder content resulted in poorer compressive properties.

The yield point values of HMMA compressed in axial direction decreased when the total CNF content was decreased (Fig. 5A and Table 4). It followed that the highest yield point of 52 kPa was observed for monoliths FZC–5, which contained the highest mass of CNF (6.6 mg/mL of suspension). The same monolith also exhibited the highest rigidity, i.e. had the highest Young's modulus of 1080 kPa. Accordingly, the lowest yield point value (2 kPa) and lowest Young's modulus (150 kPa) were obtained for the monolith containing the lowest CNF mass (FZC–9), i.e. 3.0 mg/mL of suspension (Table 1). While the decrease in yield point values was directly dependent on the absolute CNF content, Young's modulus was also influenced by MA powder content. Consequently, FZC–7 was more rigid than FZC–2 (670 kPa and 590 kPa, respectively) since the latter contained less MA powder. Still due to higher CNF content, FZC–2 had a substantially higher yield point than FZC–7 (20 kPa and 13 kPa, respectively).

For monoliths with more pronounced anisotropic structure (FZC–1, FZC–2, and FZC–5) there were big differences between compressive properties in axial and radial direction, while for monoliths with less distinct anisotropy (FZC–7 and FZC–9), the stress-strain curves and yield points obtained in both directions were much more similar (Fig. 5A and B and Table 4). For lower volume fractions ($\varphi_A < 0.054$), much better mechanical properties could be observed in axial direction. At lower volume fractions, where the pore structure is distinctively columnar,
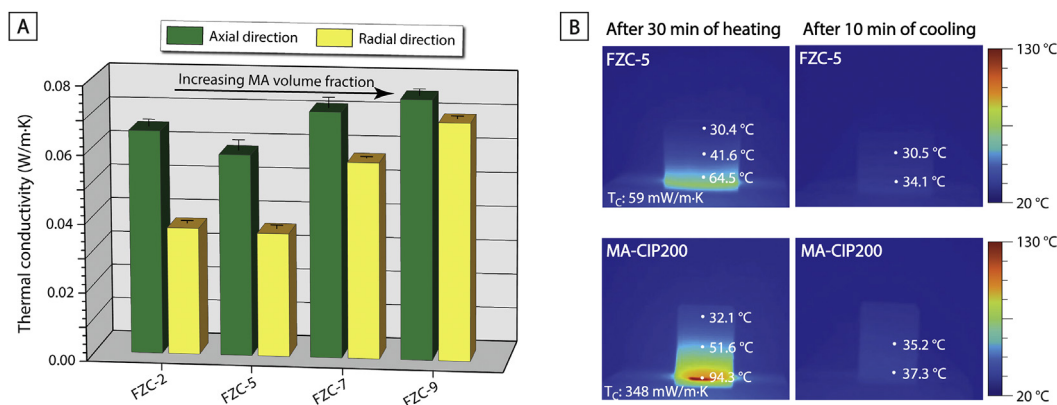
Fig. 6. A) Effective thermal conductivity (λ) of selected monoliths measured in axial and radial direction. B) Thermographic images of monoliths FZC–5 and MA–CIP200 after 30 min of heating and after 10 min of subsequent cooling down. The colors in the images show the temperature distribution on the surface of the monoliths. (For interpretation of the references to color in this figure legend, the reader is referred to the Web version of this article.)

Table 5
Summary of thermal properties of selected monoliths.

Sample	λ (axial direction)	λ (radial direction)	Specific heat capacity (c_p)
	W/m·K	W/m·K	kJ/kg·K
FZC–2	0.065 ± 0.002	0.037 ± 0.001	1.288 ± 0.007
FZC–4	0.065 ± 0.001	0.038 ± 0.001	1.224 ± 0.007
FZC–5	0.059 ± 0.003	0.037 ± 0.001	1.343 ± 0.015
FZC–7	0.072 ± 0.003	0.057 ± 0.002	1.223 ± 0.008
FZC–9	0.077 ± 0.002	0.069 ± 0.001	1.139 ± 0.008
MA–CIP200	0.327 ± 0.004	0.356 ± 0.006	1.000 ± 0.022

better mechanical properties in axial direction (parallel to pore walls) are typically observed [45]. For example, yield points of 52 kPa and 14 kPa were obtained for monolith FZC–5 ($\varphi_A = 0.027$) in axial and radial direction, respectively. There were also big differences between axial and radial Young's modulus, which was less than 50% in radial direction, i.e. 1080 kPa and 410 kPa for axial and radial direction, respectively. On the other hand, there were only slight differences between axial and radial yield points or Young's modulus at higher volume fractions. Monolith FZC–7 had yield point values at 13 kPa for axial direction and 12 kPa for radial direction, while there was a slightly bigger difference between axial and radial Young's modulus of this monolith, i.e., 670 kPa and 510 kPa, respectively.

Individual influences of CNF and MA volume fraction were also evaluated (Fig. 5C). Poor mechanical properties were observed for FZC–1 (yield point of 4 kPa), indicating that CNF showed poor mechanical properties when freeze-casted on its own, i.e. without MA powder. On the other hand, after the addition of the lowest MA volume fraction ($\varphi_A = 0.013$), the yield point increased considerably (to 20 kPa), showing that MA powder endows CNF walls with stiffness and mechanical strength. After additional increase of the volume fraction (φ_A) for 100%, i.e. from 0.013 to 0.027 (FZC–2 and FZC–4, respectively), the compressive yield point further increased for ≈35%. However, when CNF mass was increased by less than a half, i.e. from 4.6 to 6.6 mg per 1 mL of suspension (FZC–4 and FZC–5, respectively) the yield point occurred at around 90% higher stress, i.e. at 52 kPa. Indeed, while MA powder must be added in order to reinforce CNF walls, the contribution of CNF to the overall strength of HMMA monoliths is much greater than the contribution of MA powder content.

3.4. Thermal properties

The average thermal conductivity in axial direction (λ_a) of monoliths containing MA powder (FZC–2 through FZC–9) was 0.068 ± 0.009 W/

m·K which is approximately 30% lower than the thermal conductivity of sintered freeze-casted α–Al_2O_3 monoliths of comparable porosity [46]. However, the λ of HMMAs was higher than the value reported for highly porous pure CNF aerogels, which possessed considerably lower thermal conductivity, slightly below 0.04 W/m·K [47].

As can be seen from Fig. 6A, increase in the MA content from $\varphi_A = 0.013$ to 0.082 had little effect on axial thermal conductivity, which increased from 0.065 to 0.077 W/m·K (Table 5). Unlike in axial direction, thermal conductivity in radial direction (λ_r) exhibited a more pronounced dependence from MA volume fraction, i.e. an increase in λ from 0.037 to 0.057 W/m·K can be observed when φ_A is increased from 0.027 to 0.054 (monoliths FZC–5 and FZC–7, respectively). This could be explained by solid conduction of the walls [48]. Higher volume fractions lead to an increased MA particle content in monoliths pore walls. As a result, the wall thickness increased and pore diameters decreased, which led to an enhanced solid conduction of the material in radial direction and consequently higher radial thermal conductivity. On the other hand, neither λ_a nor λ_r exhibited any dependence from the MA/CNF ratio. As can be seen from Table 5 a considerable decrease of MA/CNF ratio (FZC–2, FZC–4 and FZC–5) caused practically no changes in the monoliths thermal conductivity. Thus it can be concluded that the increase of thermal conductivity is not MA/CNF-ratio-dependent, but occurred solely due to the increase of MA powder volume fraction above a certain value, i.e., 0.054.

Considerable differences between axial and radial thermal conductivity in monoliths FZC–2 and FZC–5 can be noticed. The average λ value for these two monoliths was 0.062 ± 0.003 W/m·K in axial direction, while a much lower value of 0.037 W/m·K was measured for both monoliths in radial direction (Table 5). On the other hand, there were only slight differences between radial and axial λ of monoliths FZC–7 and FZC–9, i.e. an average value of 0.063 ± 0.006 W/m·K was measured in radial direction, while the average λ in axial direction was 0.075 ± 0.003 W/m·K. The structure was distinctively anisotropic in monoliths FZC–2 and FZC–5 and consequently, due to solid conduction of the cell walls in axial direction and possibly natural convection along the same orientation, the value of λ in axial direction was higher than in radial direction. However, with increasing solid volume fraction, i.e. thickening of pore walls and decreasing of the pore diameters the structure became more isotropic and consequently only small differences between radial and axial λ values can be observed (monoliths FZC–7 and FCZ–9).

For comparison, CIP consolidated HMMA monoliths (MA–CIP200), with a porosity of 70.8% (approximately 25% lower than in the case of freeze-casted monoliths) possessed a λ of 0.327 W/m·K (Tables 2 and 5), which is more than 5-times higher than the one of FZC–5. A lower λ can be readily explained by higher porosity of freeze-casted monoliths in comparison to MA–CIP200. A qualitative representation of the thermal

conductivity of MA–CIP200 monolith was additionally obtained by thermographic imaging (Fig. 6B). Both HMMA monoliths showed a very efficient thermal insulation. While the outer layer of sample MA–CIP200 was heated to more than 90 °C, the freeze-casted monolith heated to only around 60 °C in the same time interval (30 min). In contrast, only slight differences between the final temperatures of the two monoliths could be observed after cooling down. After only 10 min, both monoliths cooled down to almost room temperature.

4. Conclusions

Freeze-casting was employed for the first time to consolidate aqueous suspensions containing mesoporous AlN-hydrolysis-derived γ–Al_2O_3 (MA). CNF and NaPAA were added to the suspensions prior to consolidation in order to prevent sedimentation and particle segregation as well as to endow green monoliths with mechanical stability not requiring additional calcination nor sintering steps. The as-prepared monoliths possessed anisotropic layered structure and displayed high, hierarchical porosity (93.1–99.2%). Macropores were in the range of 1–300 μm and shaped as columnar structures, while mesopores, had an average diameter of 6 nm all contributing to a hierarchical macro- and meso-porous alumina (HMMA) monoliths.

HMMA monoliths thus exhibited relatively high permeability and high surface area (91–138 m^2/g). Additionally, they also exhibited low, anisotropic thermal conductivity (0.036–0.077 W/m·K) and compressive strengths (up to 52 kPa) rarely seen in unsintered, highly porous materials. The ratio MA/CNF and freeze rate had a profound influence on the surface area, porosity and compressive properties. On the other hand, none of these parameters had any influence on the thermal conductivity, where its increase was observed only after a certain, high enough MA volume fraction was reached.

The interesting textural and structural properties of the CNF-reinforced HMMA monoliths could make the presented strategy for processing of hierarchically porous MA materials appealing for production of key components in salient applications like thermal management (insulative materials) and continuous flow (catalytic) processes.

Declaration of competing interest

The authors declare that they have no known competing financial interests or personal relationships that could have appeared to influence the work reported in this paper.

Acknowledgements

Appendix A. Supplementary data

Supplementary data to this article can be found online at https ://doi.org/10.1016/j.oceram.2021.100069.

References

[1] T. Ohji, M. Fukushima, Macro-porous ceramics: processing and properties, Int. Mater. Rev. 57 (2012) 115–131, https://doi.org/10.1179/1743280411Y.0000000006.

[2] P. Colombo, Conventional and novel processing methods for cellular ceramics, Philos. Trans. R. Soc. A Math. Phys. Eng. Sci. 364 (2006) 109–124, https://doi.org/10.1098/rsta.2005.1683.

[3] X. Li, M. Sun, J.C. Rooke, L. Chen, B.L. Su, Synthesis and applications of hierarchically porous catalysts, Chin. J. Catal. 34 (2013) 22–47, https://doi.org/10.1016/s1872-2067(11)60507-x.

[4] A. Corma, From microporous to mesoporous molecular sieve materials and their use in catalysis, Chem. Rev. 97 (1997) 2373–2419, https://doi.org/10.1021/cr960406n.

[5] J. Dhainaut, S. Deville, I. Amirouche, M. Klotz, A reliable method for the preparation of multiporous alumina monoliths by ice-templating, Inorganics 4 (2016) 6, https://doi.org/10.3390/inorganics4010006.

[6] S. Hartmann, A. Sachse, A. Galarneau, Challenges and strategies in the synthesis of mesoporous alumina powders and hierarchical alumina monoliths, Materials 5 (2012) 336–349, https://doi.org/10.3390/ma5020336.

[7] P.S. Liu, G.F. Chen, Fabricating porous ceramics, in: Porous Mater. Process. Appl, Butterworth-Heinemann, Oxford, 2014, pp. 221–302, https://doi.org/10.1016/B978-0-12-407788-1.00005-8.

[8] G. Busca, The surface of transitional aluminas: a critical review, Catal. Today 226 (2014) 2–13, https://doi.org/10.1016/j.cattod.2013.08.003.

[9] G. Busca, Structural, surface, and catalytic properties of aluminas, in: F.C. Jentoft (Ed.), Adv. Catal. Vol. 57, Academic Press, London, 2014, pp. 319–404, https://doi.org/10.1016/B978-0-12-800127-1.00003-5.

[10] L. Le Li, W.T. Duan, Q. Yuan, Z.X. Li, H.H. Duan, C.H. Yan, Hierarchical γ-Al_2O_3 monoliths with highly ordered 2D hexagonal mesopores in macroporous walls, Chem. Commun. (2009) 6174–6176, https://doi.org/10.1039/b912495k.

[11] K. Zhang, Z. Fu, T. Nakayama, K. Niihara, Structural evolution of hierarchical macro/mesoporous Al_2O_3 monoliths under heat-treatment, Microporous Mesoporous Mater. 153 (2012) 41–46, https://doi.org/10.1016/j.micromeso.2011.12.014.

[12] B.E. Yoldas, Alumina sol preparation from alkoxides, Am. Ceram. Soc. Bull. 54 (1975) 289–290.

[13] W. Deng, M.W. Toepke, B.H. Shanks, Surfactant-assisted synthesis of alumina with hierarchical nanopores, Adv. Funct. Mater. 13 (2003) 61–65, https://doi.org/10.1002/adfm.200390007.

[14] Y. Tokudome, K. Fujita, K. Nakanishi, K. Miura, K. Hirao, Synthesis of monolithic Al_2O_3 with well-defined macropores and mesostructured skeletons via the sol-gel process accompanied by phase separation, Chem. Mater. 19 (2007) 3393–3398, https://doi.org/10.1021/cm063051p.

[15] B. Gaweł, G. Øye, Hierarchical γ-alumina monoliths with macro- and meso porosity prepared by using cross-linked dextran gel beads as the template, Mater. Lett. 95 (2013) 86–88, https://doi.org/10.1016/j.matlet.2012.12.081.

[16] Y. Zhang, H. Liang, C.Y. Zhao, Y. Liu, Macroporous alumina monoliths prepared by filling polymer foams with alumina hydrosols, J. Mater. Sci. 44 (2009) 931–938, https://doi.org/10.1007/s10853-008-3189-6.

[17] S. Musić, D. Dragčević, S. Popović, Hydrothermal crystallization of boehmite from freshly precipitated aluminum hydroxide, Mater. Lett. 40 (1999) 269–274, https://doi.org/10.1016/S0167-577X(99)00088-9.

[18] S. Deville, Freeze-casting of porous ceramics: a review of current achievements and issues, Adv. Eng. Mater. 10 (2008) 155–169, https://doi.org/10.1002/adem.200700270.

[19] G. Frank, E. Christian, K. Dietmar, A novel production method for porous sound-absorbing ceramic material for high-temperature applications, Int. J. Appl. Ceram. Technol. 8 (2011) 646–652, https://doi.org/10.1111/j.1744-7402.2009.02479.x.

[20] S. Deville, E. Saiz, R.K. Nalla, A.P. Tomsia, Freezing as a path to build complex composites, Science 311 (2006) 515–518, https://doi.org/10.1126/science.1120937.

[21] S.M. Miller, X. Xiao, J.A. Setlock, K.T. Faber, Freeze-cast alumina pore networks: effects of processing parameters in steady-state solidification regimes of aqueous slurries, J. Eur. Ceram. Soc. 38 (2018) 5134–5143, https://doi.org/10.1016/j.jeurceramsoc.2018.07.009.

[22] D.F. Souza, E.H.M. Nunes, D.S. Pimenta, D.C.L. Vasconcelos, J.F. Nascimento, W. Grava, M. Houmard, W.L. Vasconcelos, Synthesis and structural evaluation of freeze-cast porous alumina, Mater. Char. 96 (2014) 183–195, https://doi.org/10.1016/j.matchar.2014.08.009.

[23] Y.M. Tan, O. Cervantes, S.W. Nam, J.D. Molitoris, J.P. Hooper, Dynamic fragmentation of cellular, ice-templated alumina scaffolds, J. Appl. Phys. 119 (2016), https://doi.org/10.1063/1.4939702.

[24] H.X. Zhang, C.Z. Zhao, C.Q. Hong, Aligned and porous alumina ceramics prepared by camphene-based freeze-casting route: microstructure and properties, Mater. Res. Innovat. 19 (2015) S34–S38, https://doi.org/10.1179/1432891715Z.0000000001512.

[25] W.L. Li, K. Lu, J.Y. Walz, Freeze casting of porous materials: review of critical factors in microstructure evolution, Int. Mater. Rev. 57 (2012) 37–60, https://doi.org/10.1179/1743280411Y.0000000011.

[26] F. He, W. Li, L. Yang, Z. Zhu, L. Zhou, X. Zhang, X. He, Alumina aerogels with unidirectional channels under different freezing temperatures during freeze casting—Part I: control and analysis of pore channels, Ceram. Int. 46 (2020) 13588–13598, https://doi.org/10.1016/j.ceramint.2020.02.144.

[27] A. Kocjan, The hydrolysis of AlN powder – a powerful tool in advanced materials engineering, Chem. Rec. 18 (2018) 1232–1246, https://doi.org/10.1002/tcr.201800001.

[28] A. Kocjan, A. Dakskobler, T. Kosmač, Evolution of aluminum hydroxides in diluted aqueous aluminum nitride powder suspensions, Cryst. Growth Des. 12 (2012) 1299–1307, https://doi.org/10.1021/cg201349s.

[29] A. Ojuva, F. Akhtar, A.P. Tomsia, L. Bergström, Laminated adsorbents with very rapid CO_2 uptake by freeze-casting of zeolites, ACS Appl. Mater. Interfaces 5 (2013) 2669–2676, https://doi.org/10.1021/am400122r.

[30] H. Hudelja, B. Wicklein, D. Kuščer, A. Kocjan, Triggering the aqueous interparticle association of γ–Al_2O_3 hierarchical assemblies using divalent cations and cellulose nanofibers, J. Eur. Ceram. Soc. 41 (2021) 590–598, https://doi.org/10.1016/j.scitotenv.2020.137421.

[31] Ú. Fillat, B. Wicklein, R. Martín-Sampedro, D. Ibarra, E. Ruiz-Hitzky, C. Valencia, A. Sarrión, E. Castro, M.E. Eugenio, Assessing cellulose nanofiber production from olive tree pruning residue, Carbohydr. Polym. 179 (2018) 252–261, https://doi.org/10.1016/j.carbpol.2017.09.072.

[32] A. Kocjan, T. Konegger, A. Dakskobler, Hierarchical macroporous-mesoporous gamma-alumina monolithic green bodies with high strength, J. Mater. Sci. 52 (2017) 11168–11178.

[33] M. Innocentini, P. Sepulveda, F. Ortega, Permeability, in: M. Scheffler, P. Colombo (Eds.), Cell. Ceram., Wiley, Weinheim, 2005, pp. 313–341, https://doi.org/10.1007/978-1-4614-7990-1.

[34] S. Deville, Ice-templating, freeze casting: beyond materials processing, J. Mater. Res. 28 (2013) 2202–2219, https://doi.org/10.1557/jmr.2013.105.

[35] S. Deville, E. Saiz, A.P. Tomsia, Ice-templated porous alumina structures, Acta Mater. 55 (2007) 1965–1974, https://doi.org/10.1016/j.actamat.2006.11.003.

[36] E. Munch, E. Saiz, A.P. Tomsia, S. Deville, Architectural control of freeze-cast ceramics through additives and templating, J. Am. Ceram. Soc. 92 (2009) 1534–1539, https://doi.org/10.1111/j.1551-2916.2009.03087.x.

[37] H. Sehaqui, Q. Zhou, L.A. Berglund, High-porosity aerogels of high specific surface area prepared from nanofibrillated cellulose (NFC), Compos. Sci. Technol. 71 (2011) 1593–1599, https://doi.org/10.1016/j.compscitech.2011.07.003.

[38] C. Antonini, T. Wu, T. Zimmermann, A. Kherbeche, M.J. Thoraval, G. Nyström, T. Geiger, Ultra-porous nanocellulose foams: a facile and scalable fabrication approach, Nanomaterials 9 (2019) 1–14, https://doi.org/10.3390/nano9081142.

[39] J. Kim, J.H. Ha, J. Lee, I.H. Song, Effect of pore structure on gas permeability constants of porous alumina, Ceram. Int. 45 (2019) 5231–5239, https://doi.org/10.1016/j.ceramint.2018.11.219.

[40] M. Fukushima, M. Nakata, Y. Zhou, T. Ohji, Y. Yoshizawa, Fabrication and properties of ultra highly porous silicon carbide by the gelation-freezing method, J. Eur. Ceram. Soc. 30 (2010) 2889–2896, https://doi.org/10.1016/j.jeurceramsoc.2010.03.018.

[41] D.F. Souza, E.H.M. Nunes, J.A. Queiroga, W.L. Vasconcelos, Microstructural characterization and gas permeation performance of freeze-cast alumina supports, J. Eur. Ceram. Soc. 38 (2018) 4020–4025, https://doi.org/10.1016/j.jeurceramsoc.2018.04.040.

[42] M.D.M. Innocentini, V.P. Rodrigues, R.C.O. Romano, R.G. Pileggi, G.M.C. Silva, Permeability Optimization and Performance Evaluation of Hot Aerosol Filters Made Using Foam Incorporated Alumina Suspension, vol. 162, 2009, pp. 212–221, https://doi.org/10.1016/j.jhazmat.2008.05.025.

[43] B. Yuan, J. Zhang, J. Yu, R. Song, Q. Mi, J. He, J. Zhang, Transparent and flame retardant cellulose/aluminum hydroxide nanocomposite aerogels, Sci. China Chem. 59 (2016) 1335–1341, https://doi.org/10.1007/s11426-016-0188-0.

[44] L. Wang, M. Sánchez-Soto, Green bio-based aerogels prepared from recycled cellulose fiber suspensions, RSC Adv. 5 (2015) 31384–31391, https://doi.org/10.1039/c5ra02981c.

[45] K.L. Scotti, D.C. Dunand, Freeze casting – a review of processing, microstructure and properties via the open data repository, Prog. Mater. Sci. 94 (2018) 243–305, https://doi.org/10.1016/j.pmatsci.2018.01.001.

[46] F. He, Z. Zhu, L. Yang, W. Li, X. Zhang, L. Zhou, X. He, Alumina aerogels with unidirectional channels under different freezing temperatures during freeze casting——Part II: anisotropic mechanical and thermal conductive properties, Ceram. Int. 46 (2020) 25691–25696, https://doi.org/10.1016/j.ceramint.2020.07.045.

[47] T. Wu, Z. Zeng, G. Siqueira, K. De France, D. Sivaraman, C. Schreiner, R. Figi, Q. Zhang, G. Nyström, Dual-porous cellulose nanofibril aerogels via modular drying and cross-linking, Nanoscale 12 (2020) 7383–7394, https://doi.org/10.1039/d0nr00860e.

[48] B. Wicklein, A. Kocjan, G. Salazar-Alvarez, F. Carosio, G. Camino, M. Antonietti, L. Bergström, Thermally insulating and fire-retardant lightweight anisotropic foams based on nanocellulose and graphene oxide, Nat. Nanotechnol. 10 (2015) 277–283, https://doi.org/10.1038/nnano.2014.248.